How to cite: Angew. Chem. Int. Ed. 2024, e202407228
doi.org/10.1002/anie.202407228

Solar Cells

Functionalized Thienopyrazines on NiOx Film as Self-Assembled Monolayer for Efficient Tin-Perovskite Solar Cells Using a Two-Step Method

Chun-Hsiao Kuan, Shakil N. Afraj, Yu-Ling Huang, Arulmozhi Velusamy, Cheng-Liang Liu, Ting-Yu Su, Xianyuan Jiang, Jhih-Min Lin, Ming-Chou Chen, and Eric Wei-Guang Diau**

Abstract: Three functionalized thienopyrazines (**TP**s), **TP-MN** (**1**), **TP-CA** (**2**), and **TPT-MN** (**3**) were designed and synthesized as self-assembled monolayers (SAMs) deposited on the NiOx film for tin-perovskite solar cells (TPSCs). Thermal, optical, electrochemical, morphological, crystallinity, hole mobility, and charge recombination properties, as well as DFT-derived energy levels with electrostatic surface potential mapping of these SAMs, have been thoroughly investigated and discussed. The structure of the **TP-MN** (**1**) single crystal was successfully grown and analyzed to support the uniform SAM produced on the ITO/NiOx substrate. When we used NiOx as HTM in TPSC, the device showed poor performance. To improve the efficiency of TPSC, we utilized a combination of new organic SAMs with NiOx as HTM, the TPSC device exhibited the highest PCE of 7.7 % for **TP-MN** (**1**). Hence, the designed NiOx**/TP-MN** (**1**) acts as a new model system for the development of efficient SAM-based TPSC. To the best of our knowledge, the combination of organic SAMs with anchoring CN/CN or CN/COOH groups and NiOx as HTM for TPSC has never been reported elsewhere. The TPSC device based on the NiOx**/TP-MN** bilayer exhibits great enduring stability for performance, retaining ~80 % of its original value for shelf storage over 4000 h.

Introduction

With the increasing demand for clean and renewable energy, photovoltaic technology, which directly converts solar energy into electricity, has attracted greater attention in recent years.[1–4] Perovskite solar cells (PSCs) based on metal halide perovskite materials are one of the most promising photovoltaic technologies due to the rapid development of their power conversion efficiency (PCE), up to 26.1 %,[5] with cheaper and facile solution-based fabrication process. The promise of low-cost, solution-processed PSCs with such high efficiencies and their potential impact on the global renewable-energy landscape is driving such research efforts worldwide.[6–7] Significant progress has thus been made in the up-scaling and stability of PSCs, as they are promising for commercialization.[8] However, the halide-perovskite absorber materials in the prevailing high-performance PSCs still contain toxic lead (Pb), which is a challenging issue and may limit the future commercial deployment of PSCs.[9–10] This is primarily because the use of Pb is likely to be restricted in future electronic devices because of health and ecological concerns, and the industrial-scale manufacturing of Pb-containing PSCs will entail additional handling requirements, which is likely to increase the cost substantially.[10] As such there is an urgent need to develop environmentally friendly Pb-free PSCs.[11–21] As part of this work tin-based halide perovskite solar cells (TPSCs) have attracted growing attention due to their environmental friendliness, low cost, and solution manufacturing, with reported a record PCE of 15.7 %.[22]

[*] C.-H. Kuan,[+] Y.-L. Huang, E. W.-G. Diau
Department of Applied Chemistry, and Institute of Molecular Science National Yang Ming Chiao Tung University 1001 Ta-Hseuh Rd., Hsinchu 300093, Taiwan
E-mail: diau@nycu.edu.tw

C.-H. Kuan,[+] E. W.-G. Diau
Center for Emergent Functional Matter Science National Yang Ming Chiao Tung University 1001 Ta-Hseuh Rd., Hsinchu 300093, Taiwan

S. N. Afraj,[+] A. Velusamy, T.-Y. Su, M.-C. Chen
Department of Chemistry, National Central University, 300 Zhongda Rd., Taoyuan 320317, Taiwan
E-mail: mcchen@ncu.edu.tw

C.-L. Liu
Department of Materials Science and Engineering, National Taiwan University, No. 1, Sec. 4, Roosevelt Rd., Taipei 106319, Taiwan

X. Jiang
School of Physical Science and Technology, ShanghaiTech University, Shanghai 201210, China

J.-M. Lin
National Synchrotron Radiation Research Center, 101 Hsin-Ann Road, Hsinchu Science Park, Hsinchu 300092, Taiwan

[+] C.-H. Kuan, and S. N. Afraj contributed equally to this work.

We also realize that, in the presence of ammonium-based compounds, tin may easily bio-accumulate in crops and enter the human food chain. The bio-toxicity of tin (Sn) in perovskite materials, specifically those used in perovskite solar cells, presents several significant issues. While tin is considered as a safer alternative to lead, its incorporation in perovskite structures is not free from environmental and health concerns. Here are the main points: tin ions (Sn^{2+} and Sn^{4+}) can be toxic to various forms of life, particularly aquatic organisms. They can interfere with biological processes at the cellular level. For environmental degradation and release, one of the major concerns is the stability of tin-based perovskites. These materials are prone to oxidation and degradation, which can lead to the release of tin ions or compounds into the environment. If tin perovskite solar cells are not properly encapsulated or if they degrade over time, tin can leach into the soil and water causing environmental issues.[22]

Currently, the performance of TPSC is lag behind its lead analog. However, the band gap of a tin perovskite is smaller than that of a lead perovskite, so TPSC ought to have a higher theoretical PCE than a lead-based PSC.[23–24] To enhance the performance of TPSCs, various engineering strategies were implemented to suppress Sn^{2+} oxidation, passivate surface defects, and regulate perovskite crystal formation.[24–30] In most high-efficiency TPSCs, PEDOT:PSS is typically used as the HTM through a one-step deposition process.[31–34] However, under humid conditions, the hygroscopic nature of PEDOT:PSS can readily lead to the degradation of TPSC device performance.[35] To address this issue, a two-step deposition technique was developed, allowing TPSCs to be compatible with hydrophobic HTMs such as PTAA and other polymers, thereby improving both device performance and stability.[36–39]

Recently, successful substitution of PEDOT:PSS with small organic molecules, which act as SAMs, on an ITO surface has been accomplished for TPSC.[12,13] Using SAMs as HTMs to replace PEDOT:PSS offers several benefits.[40–42] Initially, the synthesis of organic SAMs can be accomplished with great ease and at a relatively low expense.[43–44] Furthermore, the energy level of SAM molecules can be adjusted to align with that of tin perovskite. Ultimately, the SAM molecule has the ability to create a thin and precisely arranged layer between tin perovskite and ITO. This layer enhances the transfer of positive charges from perovskite to ITO and perhaps decreases the occurrence of charge recombination.[12,45–46] Several π-conjugated organic dye molecules such as **EDR03**,[42] **Br2EPT**,[46] **J2CA**[47] have been explored as potential SAMs for lead-based PSCs, and exhibit a PCE of 21.2 %, 21.8 %, and 18.82 %, respectively (Figure 1). Organic SAM molecule **OMe-2PACz** was explored for TPSC, and the PCE of 6.5 % was reported in 2021 for the first time.[12] Recently, HTMs containing dicyanovinylene or cyano-acrylic acid (anchoring groups) have been utilized for the development of lead-based PSCs, since cyano functionality can potentially act as Lewis base to passivate perovskite surface defects through forming coordination bonds with the under-coordinated Pb^{2+} ions.[9,48] In this regard, Guo and co-workers reported cyano-based **BTORC-NA** HTM with an excellent efficiency of 21.10 % and device stability in Pb-based PSCs.[49] Xue and co-workers then reported a cyano-based **D33** HTM exhibiting PCE of 17.85 % for Pb-based PSCs.[50] Pola and co-workers designed and synthesized a dicyanovinylene group containing molecules, **ICTH1** and **ICTH$_2$**, as HTMs to attain a PCE of 18.75 % and 17.91 % in Pb-based PSCs, respectively.[51] Nazeeruddin and co-workers reported cyano-based molecules **KR321** HTM for Pb-based PSCs exhibiting a PCE of 19 %.[52] This significant progress in the development of CN/CN or CN/COOH functionality containing organic molecules for Pb-based PSCs encourages us to develop new organic SAMs for TPSC.

Thienopyrazine (**TP**) is commonly used as an electron-deficient component in the production of low-bandgap semiconductors and organic photovoltaics.[53–59] Furthermore, by incorporating two alkylated phenyl rings that are larger in size and are connected to the **TP** skeleton, it became possible to prevent the aggregation of intermolecular HTM and improve the morphologies of HTM films.[6] Due to these interesting properties of the **TP** unit, our team recently reported an efficient HTM, **TP-4D**, exhibiting PCE of 20.18 % in Pb-based PSCs.[6]

Because of its low cost, stability, and ease of processing, inorganic nickel oxide (NiOx) is an ideal HTM for creating high-efficiency, stable, and large-area inverted PSCs. These devices have achieved a PCE of 21% for a Pb-based PSC.[60] Moreover, perovskite solar cells with NiOx HTMs have demonstrated some of the best stability results under various stressors, including damp heat tests, thermal cycle tests, and long-term operational stability under light and heat.[61–64] However, TPSCs fabricated on NiOx HTLs typically showed lower open-circuit voltages (V_{oc}) compared to those using PEDOT:PSS which severely restricts their PV performance enhancement and scaling of TPSCs.[65] Therefore, it is crucial to develop effective strategies to enable efficient, reliable, and scalable NiOx-based TPSCs. Recently, Zhu and co-workers introduced a **2PADBC** organic SAM into the perovskite–NiOx interface.[65] The **2PADBC** anchors under-coordinated Ni cations through phosphonic acid groups, suppressing the reaction of highly active $Ni^{\geq 3+}$ defects with perovskites, while increasing the electron density and oxidation activation energy of Sn at the perovskite interface, reducing the interfacial nonradiative recombination caused by tetravalent Sn-defects. Passivation of reactive Ni defects yields a significantly increased open-circuit voltage from 0.712 to 0.825V, boosting the PCE to 14.19 % for the small-area device, and 12.05 % for the large-area **2PADBC** NiOx-based TPSC device.[65]

Recently our team has successfully investigated an X-shaped organic SAM and utilized it as an HTM for TPSC to achieve the best PCE of 8.3 %.[11] Thus, in continuing efforts and inspired by the above findings to develop TPSCs, in this work, we studied the modification of a NiOx/HTM layer with three organic SAMs. Herein, we have synthesized three new functionalized thienopyrazines, **TP-MN** (**1**), **TP-CA** (**2**), and **TPT-MN** (**3**) SAMs for TPSC. In the design concept of these SAMs, **TP** units are used as the central building block end-capped with **MN** or **CA** to make SAMs **1**–**3**. The

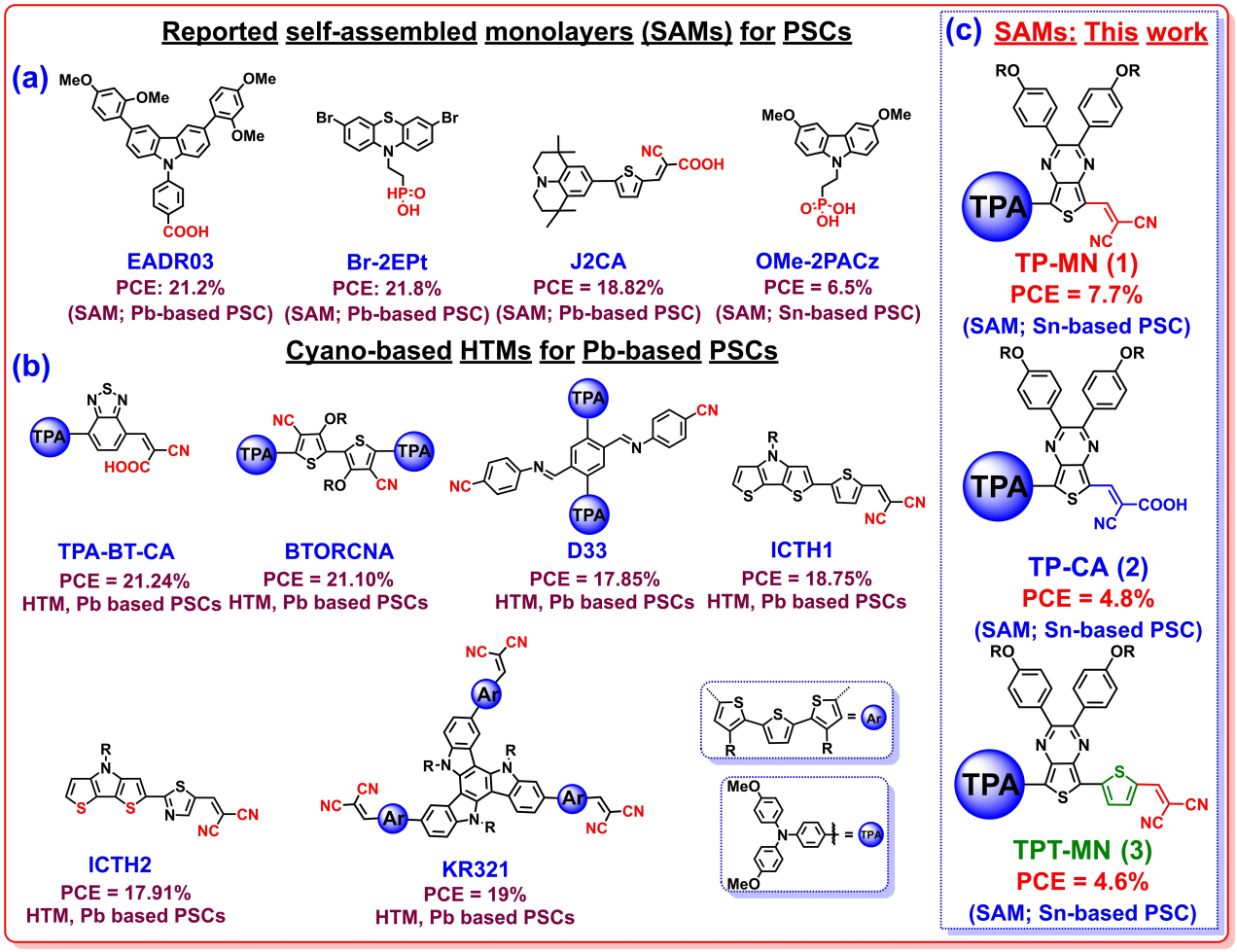

Figure 1. (a) Chemical structure of reported self-assembled monolayers (SAMs) for the PSCs. (b) Reported cyano-based HTMs for Pb-based PSCs. (c) SAMs; **TP-MN** (**1**), **TP-CA** (**2**), and **TPT-MN** (**3**) for Sn-based PSCs studied in this work.

thermal, optical, and electrochemical properties of SAM **1**–**3** are investigated. DFT-derived energy levels with electrostatic surface potential mapping of the new SAMs have been thoroughly investigated to understand the location of high electron density in the designed SAM structures. In our further investigation, when we used NiOx as the HTM in TPSC the device delivered very poor PCE. To improve the efficiency of TPSC we utilized a combination of new organic SAMs **1**–**3** with NiOx HTM, the TPSC devices based on NiOx/**TP-MN**, NiOx/**TP-CA**, and NiOx/**TPT-MN** combinations exhibited a PCE of 7.7 %, 4.8 %, and 4.6 %, respectively. To the best of our knowledge, the combination of organic SAMs with anchoring CN/CN or CN/COOH groups, and NiOx HTM for TPSC, has never been reported. This method of combining organic SAMs with NiOx HTM thus provides a good modification methodology for the future development of SAM-based TPSC. Interestingly, the device based on the NiOx/**TP-MN** bilayer exhibits great enduring stability for the performance, retaining ~80 % of its original values for shelf storage over 4000 h.

Results and Discussion

The synthetic routes for preparing **TP**-based SAMs; **1**–**3** are shown in Scheme 1 (see experimental section in the Supporting Information for details). Intermediates **4** and **5** were synthesized via Stille coupling of **TP/TPT**-based bromo-intermediate **6**–**7** with stannylated 4,4′-dimethoxytriphenylamine in the presence of $Pd(PPh_3)_4$ catalyst in the good yield. Next, SAMs TP-**MN** (**1**) and **TPT-MN** (**3**) are prepared by Knoevenagel condensation of TP-based aldehydes **4** and **5** with malononitrile and pyridine in chloroform in a good yield (~75 %).[11] Similarly, TP-based aldehyde **4** was treated with **2**-cyanoacetic acid to give **TP-CA** (**2**). The solubility of the new SAMs **1**–**3** increases due to the presence of 4,4′-dimethoxytriphenylamine units, and anchoring groups (CN/COOH or CN/CN). For example, compounds **1**–**3** have good solubility in common organic solvents, such as chlorobenzene, chloroform, and toluene. The chemical structures of **1**–**3** were confirmed by ^{1}H and ^{13}C NMR spectroscopy and mass spectrometry (see Supporting Information).

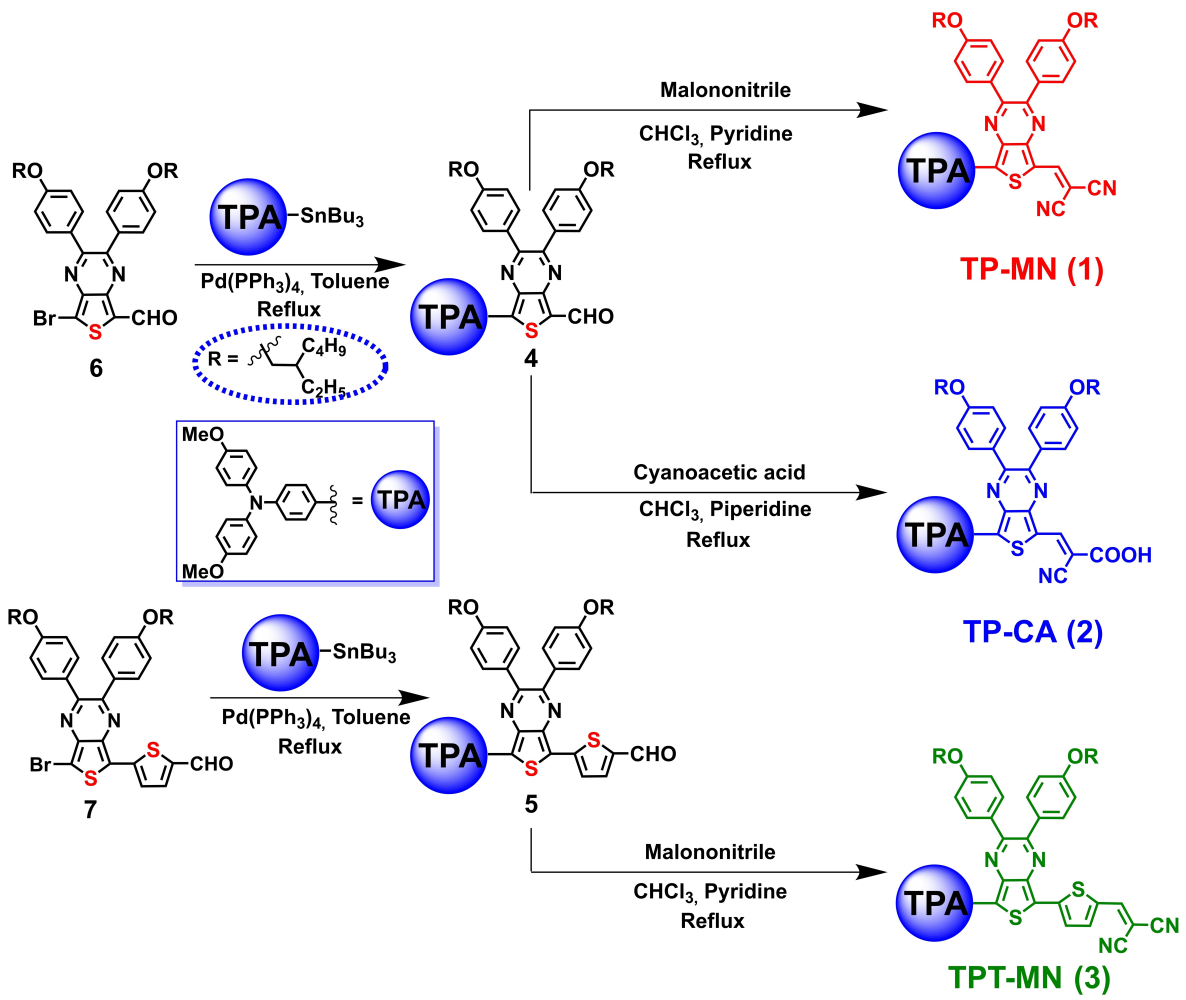

Scheme 1. Synthetic route of **TP**-based SAMs **1**–**3**.

The optical, thermal, and electrochemical properties of SAM molecules **1**–**3** are shown in Table 1. The newly synthesized molecules show good thermal stability with only ~5 % weight loss taking place at 245, 224, 212 °C for **1**–**3**, respectively, obtained by thermogravimetric analysis (TGA) (**Figure S1**, Supporting Information). TGA analysis indicates molecule **1** with methylenemalononitrile directly attached to the **TP** unit and exhibited high thermal stability as compared to compounds **2** and **3**. The ultraviolet-visible (UV/Vis) absorption spectrum of compounds **TP-MN (1)** in *o*-$C_6H_4Cl_2$ is significantly red-shifted (λ_{max} = 670 nm; Figure 2a) as compared to **TP-CA (2)** (λ_{max} = 651 nm; Figure 2a), indicating that the presence of methylenemalononitrile functionality in molecule **1** is more effective in increasing conjugation as compared to cyanoacrylic acid in molecule **2**. The absorption spectrum of compound **TPT-MN (1)** in *o*-$C_6H_4Cl_2$ is slightly red-shifted (λ_{max} = 675; Figure 2a) as compared to **TP-CA (2)** (λ_{max} = 651 nm; Figure 2a), indicating that the presence of the thiophene unit and the methylenemalononitrile functionality in molecule **3** enhances the conjugation significantly as compared to molecule **1**.[51]

The electrochemical properties of SAM molecules **1**–**3** were investigated by differential pulse voltammetry (DPV) in *o*-$C_6H_4Cl_2$ at 25 °C utilizing tetrabutylammonium hexa-

Table 1: Thermal, optical, and electrochemical properties of the indicated compounds.

SAM	T_d[a] [°C]	λ_{abs} (soln)[b] [nm]	E_{ox}[c] [V]	HOMO[d] [eV]	HOMO[e] [eV]	E_{red}[c] [V]	LUMO[d] [eV]	LUMO[e] [eV]	$\triangle Eg$[f] [eV]
TP-MN (1)	245	670	0.98	−5.42	−5.18	−0.65	−3.79	−3.55	1.63
TP-CA (2)	224	651	0.93	−5.37	−5.28	−0.78	−3.66	−3.57	1.71
TPT-MN (3)	212	675	0.83	−5.27	−5.48	−0.79	−3.65	−3.86	1.62

[a] By TGA. [b] UV-Vis absorption spectra were recorded in *o*-$C_6H_4Cl_2$. [c] By DPV in *o*-$C_6H_4Cl_2$ at 25 °C. All potentials are reported with reference to the Fc/Fc^+. [d] Calculated from equation; $E(eV) = -(4.44 + E_{ox}/E_{red}$ (vs NHE)). [e] Energy levels of thin films determined by the UPS. [f] The energy gap was calculated from the difference between HOMO and LUMO energy levels.

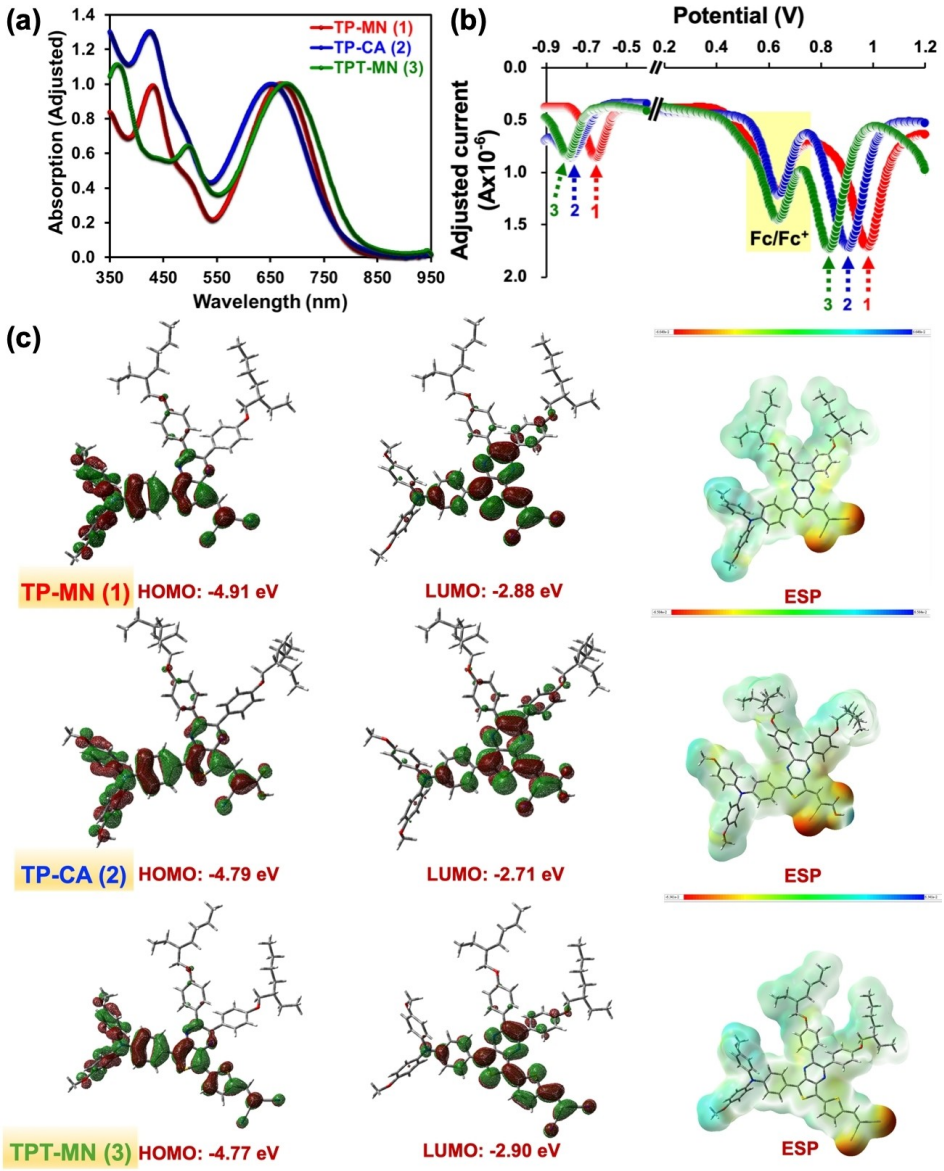

Figure 2. (a) UV/Vis absorption spectra of compounds **1–3** in *o*-$C_6H_4Cl_2$. (b) DPV response curves of **1–3**. (c) DFT-derived energy levels and electrostatic surface potential (ESP) mapping of **1–3**.

fluorophosphate as the electrolyte[66–68] (Figure 2b). The oxidation potentials of SAMs **1–3** were calibrated employing ferrocene as an internal standard at +0.64V (*vs* NHE). The HOMO/LUMO energy levels of the SAM molecules **1–3** were calculated by the equation $E(eV) = -(4.44 + E_{ox}/E_{red})$. The oxidation and reduction (Figure S2) peaks of SAM molecules **1–3** are located at +0.98/−0.65V, +0.93/−0.78V, and +0.83/−0.79V, respectively, and the derived E_{HOMO}/E_{LUMO} of compounds **1–3** are thus estimated as −5.42/−3.79 eV, −5.37/−3.66 eV, −5.27/−3.65 eV, respectively.[69] As expected, the longer conjugated **TPT-MN** (**3**) exhibits the highest HOMO and LUMO. With two strong electron-withdrawing CN groups anchored, **TP-MN** (**1**) shows the lowest HOMO and LUMO among the studied series. The energy gaps of three TPs derived from DPV are confirmed in the order of **3** (1.62 eV) < **1** (1.63 eV) < **2** (1.71 eV), which the trend is consistent with the absorption spectra shown in Figure 2a.

In order to gain a more comprehensive understanding of the electronic structures of **1-3**, we conducted DFT calculations using the Gaussian 03W software with the B3LYP/6-31G* level of theory. Figure 2c demonstrates that the HOMOs of SAM **1-3** are mostly concentrated on the TPA and extend to the phenyl units. On the other hand, the LUMOs are predominantly located on the CN/COOH anchoring groups and spread to the thienopyarazine backbone. The DFT-derived E_{HOMO} are −4.91, −4.79, and −4.77 eV for **1–3**, respectively, and the E_{LUMO} are −2.88, −2.71 and −2.90 eV for **1–3**, respectively. As calculated, longer conjugated **TPT-MN** (**3**) exhibits the highest HOMO and LUMO. In contrast, **TP-MN** (**1**) anchored by two strong electron withdrawing CN groups presents the lowest

HOMO and LUMO. The DFT-derived energy gap trend (**3** (1.87 eV) < **1** (2.03 eV) < **2** (2.08 eV)) is well-matched to that obtained from the electrochemical DPV measurement (see above). The energy levels predicted by the DFT calculations are higher than those determined by the experimentally measured electrochemical data (DPV) because of two reasons. First, the DFT results predict the electronic structures of SAM molecules in gas phase while those obtained experimentally (DPV) are in solution with 0.1 M tetrabutylammonium hexafluorophosphate electrolyte. Second, the theoretical calculation might involve certain uncertainty so that only a qualitative comparison should be made. Due to the varying environmental conditions under which DFT computations and DPV measurements are conducted, it is usual to observe slight deviations in energy trends between these two measurements.[70]

Furthermore, to enhance comprehension of the charge distribution of the SAMs and determine the appropriate groups that may securely attach to the ITO/NiOx surface, we conducted an assessment of the electrostatic surface potential (ESP) mapping for three TP molecules. Figure 2c demonstrates that when TPA units are attached to the right side of the thienopyrazine center, all SAMs exhibit localized electronic distributions on the TPA units. This allows the TPA units to supply electrons to the perovskite layer. When CN or COOH anchoring units are present on the left side of TP molecules, the electron densities (negative charges) are mostly concentrated on these terminal groups. This makes them well-suited for establishing optimal connections with the ITO/NiOx surface, facilitating the creation of self-assembled monolayers.

To gain a deeper insight into the structure of these three quite soluble TP-based SAMs, which with two branched-C_8H_{17} attached, numerous efforts to obtain their crystals have been attempted. Fortunately, the crystal of the best performance **TP-MN** (**1**) was obtained from a slow solvent diffusion method. Thus, understanding the molecular packing and arrangement of **TP-MN** on the NiOx/ITO surface becomes viable. In contrast, the single crystals of **2** and **3** cannot be obtained using the same method and this also revealed the difficulty of these two molecules forming good arrangement as SAMs on the NiOx/ITO surface, which might plausibly lead to their poorer device performance (see below). The diffraction-derived single crystal structure of **TP-MN** (**1**) molecule is presented in Figure 3 with the structural parameters summarized in **Table S1**. These results indicate that the **TP-MN** molecule crystallizes in the trigonal system with R-3 space group. Figure 3a illustrates a wide dihedral angle of 118.3° between the **TPA** and alkoxy phenyl moieties, while the SAM molecule stands upright with two CN groups serving as the anchoring points. Moreover, intramolecular interactions of 2.40Å for N–H and 2.59Å for S–H are revealed, which could induce a highly ordered one-dimensional assembly that favors a dense, tilted, highly ordered monolayer on the substrate. As shown in Figure 3b, the short double bond characteristic of 1.36Å for CA=CB, along with the relatively small twisted angles of the **TP** core to the **MN** (18.4°) and phenyl (11.8°) moieties, confirms the good π-conjugation between the central **TP**

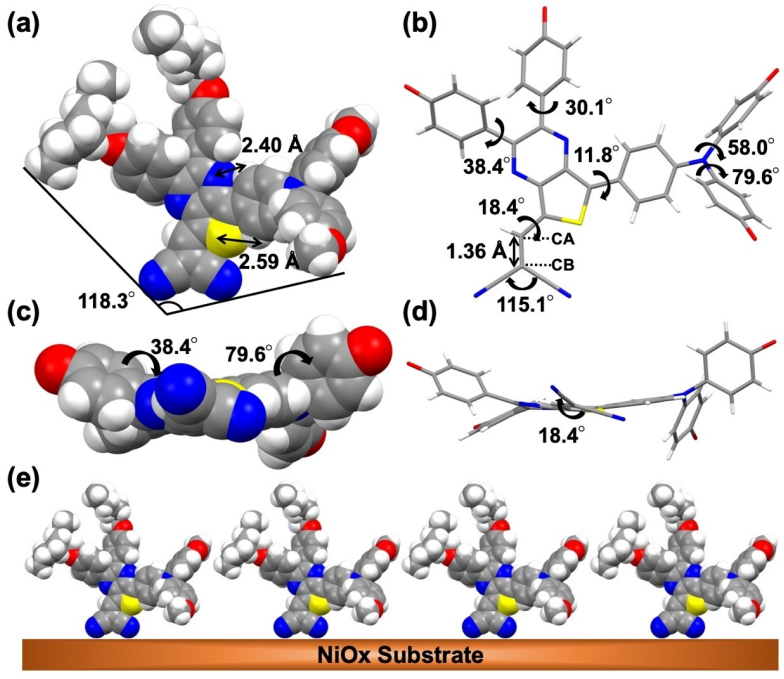

Figure 3. Crystal structure of compound TP-MN (**1**). (a) Top view of TP-MN molecule with intramolecular interactions and wide dihedral angle measured between TPA and alkoxy phenyl moieties in space filling model. (b) Top view of TP-MN molecule with various twisted angles in stick model with bC_8H_{17} and CH_3 groups omitted for clarity; (c–d) Front views of TP-MN molecule in space filling and stick models, respectively, with bC_8H_{17} and CH_3 groups omitted for clarity. (e) Proposed packing pattern of SAM on NiOx/ITO substrate.

core and the two end-anchoring CNs, which facilitates efficient charge transport. Furthermore, the two alkoxy phenyl rings on the central **TP** core exhibit less twisting (38.4° and 30.1°) compared to the two methoxy phenyl rings on the **TPA** core (79.6° and 58.0°). The presence of these twisted angles in the **TP-MN** molecule enhances solubility, enabling facile device fabrication via solution processing, thus yielding high-quality films for high PCE. In addition, the wide-angle (115.1°) between the two CN anchoring groups should benefit the SAM molecule in standing firmly on the NiOx substrate. Figure 3c–d showcases the front views of **TP-MN** molecule with obvious twisted angles of phenyl rings and anchoring groups to the central **TP** core. Based on the isolated crystal structure of TP-MN, a proposed packing pattern of this SAM on the NiOx substrate is demonstrated in Figure 3e, promoting efficient charge transfer for high-performance TPSCs. Nevertheless, TP-MN might deposit with a different geometry when it interacts with the NiOx surface.

We hypothesize that NiOx prompts the oxidation of tin perovskite, primarily occurring at the boundary between perovskite and NiOx, consequently creating a barrier that impedes the extraction of holes. Figure 4 illustrates the wettability and crystal morphology of tin perovskites deposited on NiOx and on NiOx with various SAMs. Initially, NiOx/SAM layers were deposited onto ITO substrates through dipping. NiOx is used with the aim of enhancing their hydrophilicity. The resultant contact angles for the SnI_2 precursor solution on SAM films, including **TP-MN** (19.22°), **TP-CA** (28.05°), and **TPT-MN** (24.69°), are displayed in Figures S3a–c. NiOx modification with SAMs markedly increased the hydrophilicity for **TP-MN** ($12.31° < 19.22°$), **TP-CA** ($21.38° < 28.05°$), and **TPT-MN** ($7.02° < 24.69°$), whereas the contact angle of the NiOx-only film showed a small value (7.2°), as shown in Figures 4a–d. This surface modification effect efficiently aids in the subsequent deposition of FAI to form $FASnI_3$ perovskites with a desirable morphology. This enhancement in hydrophilicity and the effect of solution processability of the SAMs on device efficiency suggests a correlation between the processability of the SAMs and their performance in devices, highlighting that only those SAMs with optimal processability achieve superior device performance. Among the SAMs, NiOx/**TP-MN** and NiOx/**TPT-MN** exhibited lower contact angles than that of NiOx/**TP-CA**.

Scanning electron microscopy (SEM) and atomic force microscopy (AFM) were employed to examine the morphologies of the tin perovskite films deposited on various NiOx/SAMs. Figures 4e–h and Figures 4m–p show top-view and cross-section SEM images of the perovskite films on differ-

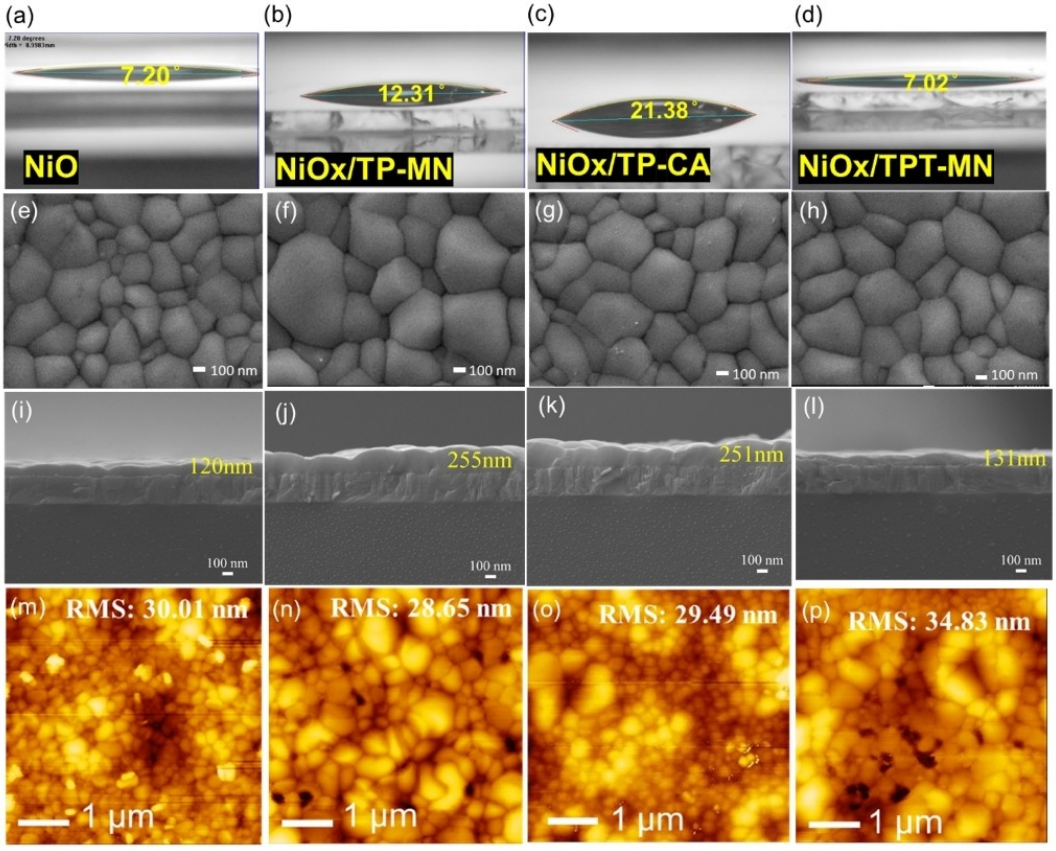

Figure 4. (a–d) Contact angles of perovskite precursor SnI_2 on varied substrates as indicated, (e–h) top-view SEM images of the corresponding perovskite films on varied substrates, (i–l) side-view SEM images of the corresponding perovskite films on varied substrates, and (m–p) AFM images of the corresponding perovskite films on varied substrates.

ent NiOx/SAMs, where the film of perovskite on SAM **TP-MN** (Figure 4f) showed larger and more uniform crystal grains than the others, consistent with the AFM findings shown in Figures 4m–p. These AFM images were analyzed to evaluate the surface roughness of the tin perovskites on various NiOx/SAMs, revealing that NiOx with **TP-MN**-based perovskites exhibited lower film roughness than the others. Figure S4 shows AFM images of the SAMs deposited on ITO (a–d) and on the NiOx/ITO (e–h) substrates. NiOx is a nanoscale particle that inherently contains some oxygen vacancies. These vacancy defects can oxidize SnI_2, leading to the creation of SnI_4 within the perovskite film. However, when NiOx is modified with SAM molecules reported in this work, these surface vacancies are effectively eliminated. This modification passivates the NiOx, preventing the oxidation of SnI_2 and thereby reducing the formation of defects. This passivation is critical for improving the overall stability and performance of the tin perovskite solar cells. Furthermore, when NiOx is employed to modify ITO, it effectively fills the small gaps on the ITO surface, thereby enhancing its overall uniformity and surface roughness. This modification leads to a more reliable and stable base for depositing subsequent layers in device fabrication. Moreover, NiOx possesses a higher density of hydroxyl (−OH) groups compared to ITO. These -OH groups are crucial as they facilitate better adhesion and interaction with other materials, which is essential during the fabrication process of the photovoltaic devices.[71–72]

The XPS spectra of Ni 2p recorded from ITO/NiOx and the SAM-modified ITO/NiOx films are shown in Figure S5. The characteristic peaks are present in all the samples, except with slight variations in the integrated area under the deconvoluted peaks. Note that some reports based on NiOx nanoparticles display that presence of Ni^{4+} at around 857.1 eV,[73] while others do not.[74] In our spectra, we observed that the Ni^{4+} peak contribution is either negligible or completely absent. The contribution from Ni^{3+} relative to Ni^{2+} is beneficial for hole transport, and the deconvoluted spectra reveal that we have greater Ni^{3+} component than Ni^{2+}. Upon SAM modification, we expect greater changes in the oxygen species and hence O 1s spectra was recorded from the samples. The normalized XPS spectra of O 1s recorded from ITO/NiOx and SAM-modified ITO/NiOx are shown in Figures 5e–h. Significant modulations in the spectra was observed, especially pertaining to the peak centered around 531 eV. This peak is assigned to the Ni-OH bonding, for which the substantial enhancements in the SAM-modified ITO/NiOx substrates imply the extent of surface coverage of NiOx with the SAM molecules. Note that there is a slight peak broadening in NiOx giving rise to an observable peak doublet at around 532 eV, which is assigned to Ni^{3+}-O. This peak doublet feature is less obvious on the SAM-modified samples in comparison to that in NiOx. It has been reported that NiOx nanoparticles treated with H_2O_2 led to significant enhancement in this peak due to the transition of $Ni(OH)_2$ to NiOOH that resulted in improved conductivity.[75] However, upon SAM-modification, our samples failed to show such an enhanced characteristic. Thus, the interlayer between the SAM and ITO is NiOx nanoparticle based, perhaps with very minor amount of NiOOH, rather than NiOx itself.

The SAM-sensitized ITO substrates display a sheet-like configuration whereas SAM-sensitized NiOx/ITO substrates manifest a compact spherical form. This variation in structure enables the latter to possess an increased specific surface area to form a compact and uniform interlayer between NiOx/ITO and perovskite.

X-ray diffraction (XRD) patterns for the tin perovskites on different SAMs (Figure 5a) suggest a slight shift toward a small angle when the perovskites were deposited on various SAMs. This alteration in the diffraction peak initially serves to negate the impact of the film strain variations due to the differing thermal expansion coefficients at the buried interface. Given that SAMs possess a lower thermal expansion coefficient compared to NiOx, it is predisposed to generating tensile strain within the film, thereby shifting the diffraction peak towards a lower angle. We deduce that the modification in the diffraction peak's position is attributable to the oxidation of Sn^{2+}, aligning with findings from previous studies.[64] The findings indicate that the SAMs engage with the perovskite by electron donation, successfully preventing oxidation and defect formation at the buried interface without compromising the perovskite's bulk structures and optical characteristics. A high-resolution grazing incidence wide-angle X-ray scattering (GIWAXS) image, demonstrating the arrangement and crystallinity of perovskites at an incident angle of 0.02°, is shown in Figure 5b for the NiOx/**TP-MN** film. Compared with perovskites based on NiOx, NiOx/**TP-CA**, and NiOx/**TPT-MN**, the perovskite on NiOx/**TP-MN** exhibits higher crystallinity as shown in Figures 5b and S6. This enhanced crystallinity improves carrier transport and boosts device performance for the NiOx/**TP-MN** device.

The hole-extraction capabilities were measured using the time-correlated single-photon counting (TCSPC) technique with excitation at 635 nm from the glass side for tin perovskite films deposited on varied SAMs; the corresponding PL decay profiles are shown in Figure 5c. The decay profiles for all conditions were fitted by a bi-exponential function. The decay rates demonstrate that NiOx/**TP-MN** exhibits the fastest hole-extraction rate, indicating the great ability of the NiOx/**TP-MN** film for hole extraction. Space-charge limited current (SCLC) measurements of the hole mobilities for the NiOx/SAM thin films revealed that NiOx/**TP-MN** has the highest hole mobility (Figure 5d), underscoring its superior performance among the other SAMs.

Using a two-step fabrication approach, TPSCs were assembled with a structure of ITO/NiOx/SAM/$FASnI_3$/C60/BCP/Ag. *J–V* characteristic measurements, as depicted in Figure 5e, reveal that the NiOx/SAMs devices perform in the following descending order: **TP-MN** (7.7 %) leads, followed by TP-CA (4.8 %), TPT-MN (4.6 %), and then NiOx-only (3.2 %) with detailed photovoltaic parameters listed in Table S3. This performance trend correlates with the morphological characteristics highlighted in Figure 4, where devices based on NiOx with **TP-CA** and **TPT-MN** lagged due to their poorer morphology, as evidenced in the AFM (Figures 4m-4p) and SEM images (Figures 4e–4h).

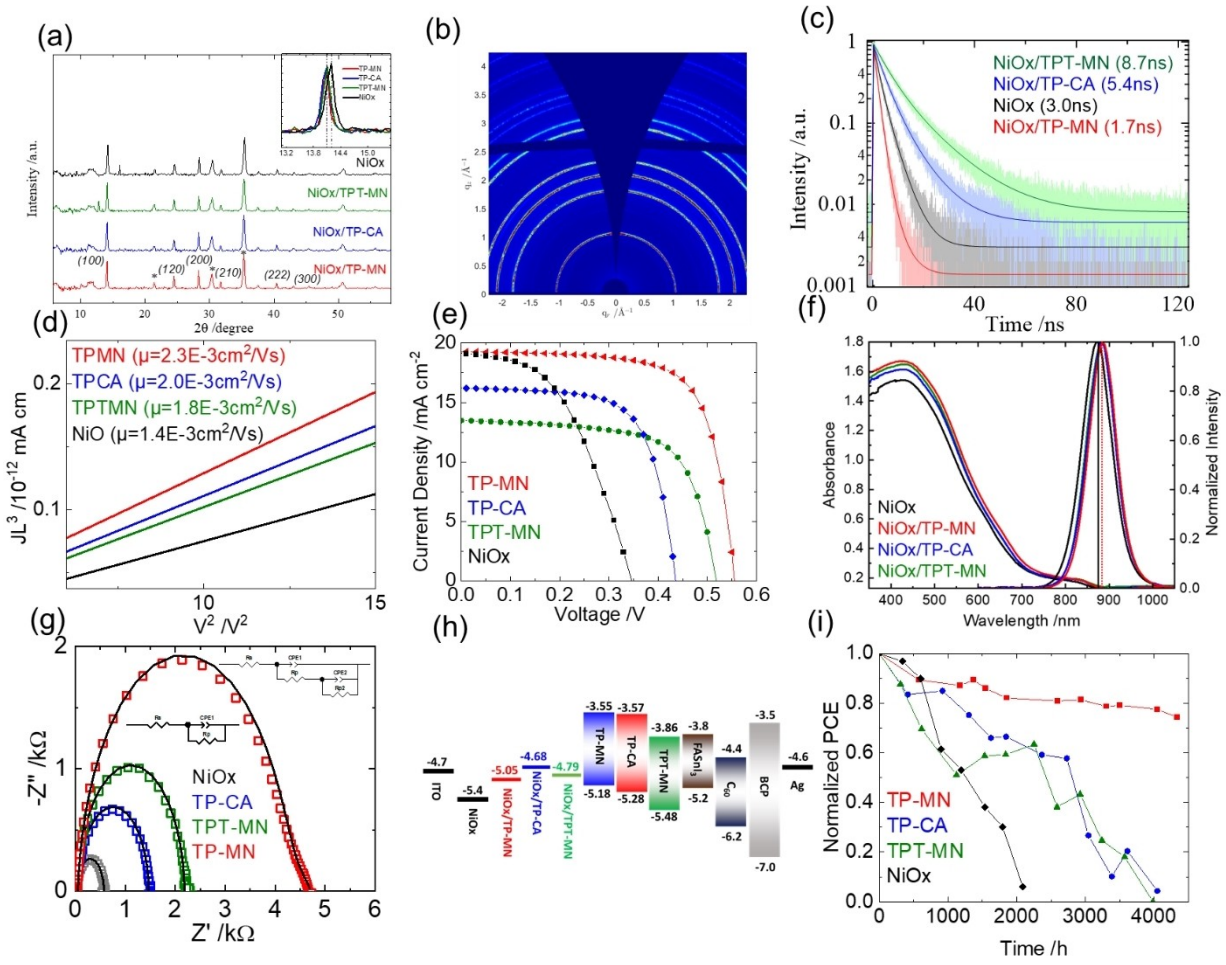

Figure 5. (a) XRD of tin perovskites on NiOx with various SAMs as indicated, and (b) GIWAXS of tin perovskite on NiOx/**TP-MN**, (c) PL decay profiles via TCSPC, (d) SCLC of tin perovskites on NiOx with various SAMs as indicated, (e) *J–V* characteristic curves, (f) UV/Vis and PL of tin perovskites on NiOx with various SAMs as indicated, (g) EIS Nyquist plots for the devices made of tin perovskites deposited on NiOx with various SAMs as indicated; (h) energy-level diagram, (i) long-term stability for the devices made of NiOx with various SAMs as indicated. The best performance is the NiOx/**TP-MN** device with PCE of 7.7%.

The superior efficiency (PCE = 7.7%) of the NiOx/**TP-MN** device is attributed to its optimal film morphology and thickness (Figures 4b/f/j/n), rapid hole extraction (Figure 5c), and improved hole mobility (Figure 5d). The incident photon-to-current conversion efficiency (IPCE) spectra for the NiOx with various SAM devices, shown in Figure S7, along with the integrated short-circuit current densities (J_{sc}), consistent with the findings from the *J–V* curves (Figure 5e), which aligns with its IPCE response, especially in the 350–700 nm spectral range, matching its absorption profile (Figure 5f).

Electrochemical impedance spectroscopy (EIS) was employed to examine the charge recombination characteristics in NiOx/SAM TPSCs compared to the NiOx-only devices, conducted in darkness at the open-circuit condition. As the Nyquist plots shown in Figure 5g, equivalent circuit-1 was used to fit the NiOx, **TP-CA**, and **TPT-MN** data, while equivalent circuit-2 was used to fit the data obtained from **TP-MN**; the corresponding fitted parameters are tableted in Tables S4–8. The sequence of charge recombination resistances reflects the V_{oc} values, with the order of NiOx/**TP-MN** > NiOx/**TPT-MN** > NiOx/**TP-CA** > NiOx-only, which is consistent with the trend of V_{oc} showing the same order. This indicates the exceptional performance of the NiOx/**TP-MN** device due to the large charge recombination resistance, which also supports its highest V_{oc} value among the other devices.

To elucidate the valence band maximum (VBM) and conduction band minimum (CBM) energy levels of each SAM and NiOx/SAM, ultraviolet photoelectron spectroscopy (UPS) and UV/Vis spectroscopy were utilized, with the UPS results with and without NiOx illustrated in Figures S8 and S9, respectively. Figure 5h shows the energy-level diagram for all SAMs with and without NiOx. It is apparent that the SAMs with NiOx modification show higher HOMO levels than those without NiOx, with the energy level of the NiOx/**TP-MN** film well matching that of $FASnI_3$, thereby supporting the observed device performances shown in Figure 5e. The VBM of NiOx is −5.4 eV, which shows a significant mismatch with that of tin perovskite (−5.2 eV).

This energy level misalignment results in poor hole mobility, as observed in SCLC measurements, leading to poor device performance. When comparing energy levels for the NiOx/SAM samples, the HOMO of NiOx/**TPT-MN** is −4.79 eV. Despite this being a better match than NiOx alone, the alignment is still less favorable compared to NiOx/**TP-MN**, resulting in lower open-circuit voltage (V_{oc}) and reduced recombination resistance. Furthermore, the HOMO of NiOx/TP-CA is higher than that of ITO, which further reduces recombination resistance and V_{oc}, consistent with the *JV* curves shown in Figure 5e.

Figure 5i compares the shelf-storage performance stability of all NiOx/SAM's TPSCs, including those based on NiOx-only device, revealing a gradual performance decline for the NiOx-based TPSC over 4000 h. The performance of the NiOx-only device degraded to naught over 2000 h, whereas the performances of the NiOx/**TP-CA** and NiOx/**TPT-MN** devices gradually declined to naught over 4000 h. In contrast, the NiOx/**TP-MN** device demonstrated exceptional long-term stability, maintaining around 80 % of its initial efficiency over 4000 h. The remarkable long-term stability of the NiOx/**TP-MN** device can be attributed to its excellent optoelectronic, morphological, crystallinity, and mobility properties as discussed previously. The reproducibility of these results was confirmed through performance statistics of 15 devices for each SAM, with the raw data summarized in Tables S9–S11 and in the boxplot form presented in Figure S10. The NiOx/**TP-MN** device also showed no effect of hysteresis, as the *J–V* scan curves show in Figure S11. Additionally, the performance at the maximum-power point (MPP) was studied for the all devices without encapsulation under one-sun illumination in ambient air conditions. We found that the **TP-MN** device has declined to 85 % of its initial value while the NiOx device has declined to 65 % of its original value. This MPP tracking results further confirm the superior stability of **TP-MN** under light-soaking conditions. In this work, the NiOx interlayer plays an important role for SAM functionalization to grow large perovskite grains with excellent uniformity and crystallinity for TPSC. The performance comparison for the SAM devices with and without a NiOx interlayer is shown in Figure S13, for which SAM devices with NiOx modification exhibited much greater performance than the SAM devices without NiOx. In addition, different concentration test is shown in the Figure S14, it clearly demonstrates that the concentration of 0.02mM yields the best photovoltaic performance, achieving the highest current density and operating voltage. This optimized concentration enhances the crystallinity and carrier transport within the perovskite layer, leading to superior device performance. Concentrations higher or lower than 0.02mM result in reduced efficiency, highlighting the importance of precise concentration to control tin perovskite solar cell fabrication.

Conclusions

Three thienopyrazines (**TP**)-based molecules, **TP-MN (1)**, **TP-CA (2)**, and **TPT-MN (3)**, were designed and synthesized as SAMs for tin-based perovskite solar cells. Functional CN/CN (**TP-MN**; **1** and **TPT-MN**; **3**) and CN/COOH (**TP-CA; 1**) groups are conjugated with **TP** or π-extended thienopyrazines (**TPT**) units to serve as the anchoring group to bond on the NiOx/ITO surface, while the triphenylamine (TPA) groups were attached to the other side of **TP** to effectively donate electrons to the perovskite layer, and both were confirmed by the DFT calculations. In addition, two soluble phenoxy groups attached to **TP** units are expected to suppress the aggregation of the dyes to some extent on the NiOx/ITO substrates. We found that both CN/CN and CN/COOH were good anchoring groups for the three organic molecules to form SAMs on the ITO/NiOx surface, and to form the smooth and uniform tin perovskite nanocrystals with excellent morphology, crystallinity, and film roughness. When we used NiOx as HTM in a TPSC, the device delivered a poor PCE of 4.0 %. To improve the efficiency of the TPSC, we further utilized a combination of new organic SAMs **1–3** with NiOx HTM. The TPSC devices based on NiOx/**TP-MN**, NiOx/**TP-CA**, and NiOx/**TPT-MN** combinations exhibited PCEs of 7.7 %, 4.8 %, and 4.6 %, respectively. SEM, AFM, XRD, GIWAXS, TCSPC, UPS, SCLC, and EIS characterizations were performed for the thin-film samples or devices under investigation to understand the optoelectronic and photovoltaic properties of this series of SAM and NiOx/SAM combination. The structure of the single crystal of the **TP-MN** molecule was obtained to support that these molecules (**1–3**) would form uniform SAM on the ITO/NiOx surface without the issue of dye aggregation. Finally, a device based on the NiOx/**TP-MN** bilayer exhibits great enduring stability for the performance, retaining ~80 % of the original values for shelf storage over 4000 h. Therefore, this method of combining organic SAMs with NiOx HTM provides a good research direction for TPSC to achieve high performance with excellent stability.

Notes

Authors declare no competing financial.

Acknowledgements

We gratefully acknowledge the support by the National Science and Technology Council (NSTC), Taiwan (grant No. MOST 111-2113-M-008-004-MY3, NSTC 111-2634-F-A49-007, NSTC 111-2123-M-A49-001 and NSTC 112-2639-M-A49-001-ASP), the Center for Emergent Functional Matter Science of National Yang-Ming Chiao-Tung University (NYCU) from the Featured Areas Research Center Program within the framework of the Higher Education Sprout Project by the Ministry of Education (MOE) in Taiwan. We also thank Ms Pei-Lin Chen (Instrumentation Center at NTHU) for Single Crystal X-ray Diffractometer analysis. We thank Dr. Y.-W. Tsai and Dr. J.-M. Lin (TPS 25A1, NSRRC) for their kind assistance in GIWAXS data analysis. We also thank Dr. B.-H. Liu and Dr. C.-H. Wang

(TLS 24A1, NSRRC) for their kind assistance in UPS data analysis.

Conflict of Interest

The authors declare no conflict of interest.

Data Availability Statement

Research data are not shared.

Keywords: Self-assembled monolayers · thienopyrazines · cyano functionality · tin perovskite · solar cells

[1] S. Zhou, S. Fu, C. Wang, W. Meng, J. Zhou, Y. Zou, Q. Lin, L. Huang, W. Zhang, G. Zeng, *Nature* **2023**, *624*, 69–73.
[2] M. Li, M. Liu, F. Qi, F. R. Lin, A. K.-Y. Jen, *Chem. Rev.* **2024**.
[3] E. W.-G. Diau, *ACS Energy Lett.* **2017**, *2*, 334–335.
[4] C. Zhu, J. Jin, Z. Wang, Z. Xu, M. C. Folgueras, Y. Jiang, C. B. Uzundal, H. K. Le, F. Wang, X. Zheng, *Science* **2024**, *383*, 86–93.
[5] Best Research-Cell Efficiency Chart. https://www.nrel.gov/pv/cell-efficiency.html (accessed 2023-07-10).
[6] S. N. Afraj, D. Zheng, A. Velusamy, W. Ke, S. Cuthriell, X. Zhang, Y. Chen, C. Lin, J.-S. Ni, M. R. Wasielewski, W. Huang, J. Yu, C.-H. Pan, R. D. Schaller, M.-C. Chen, M. G. Kanatzidis, A. Facchetti, T. J. Marks, *ACS Energy Lett.* **2022**, *7*, 2118–2127.
[7] A. Velusamy, S. Yau, C. L. Liu, Y. Ezhumalai, P. Kumaresan, M. C. Chen, *Journal of the Chinese Chemical Society* **2023**, *70*, 2046–2063.
[8] P. Murugan, T. Hu, X. Hu, Y. Chen, *J. Mater. Chem. A* **2022**, *10*, 5044–5081.
[9] S. N. Afraj, A. Velusamy, C.-Y. Chen, J.-S. Ni, Y. Ezhumalai, C.-H. Pan, K.-Y. Chen, S.-L. Yau, C.-L. Liu, C.-H. Chiang, *J. Mater. Chem. A* **2022**, *10*, 11254–11267.
[10] P. Yan, D. Yang, H. Wang, S. Yang, Z. Ge, *Energy Environ. Sci.* **2022**, *15*, 3630–3669.
[11] S. N. Afraj, C. H. Kuan, J. S. Lin, J. S. Ni, A. Velusamy, M. C. Chen, E. W.G. Diau, *Adv. Funct. Mater.* **2023**, *33*, 2213939.
[12] D. Song, S. Narra, M.-Y. Li, J.-S. Lin, E. W.-G. Diau, *ACS Energy Lett.* **2021**, *6*, 4179–4186.
[13] C.-H. Kuan, J.-M. Chih, Y.-C. Chen, B.-H. Liu, C.-H. Wang, C.-H. Hou, J.-J. Shyue, E. W.-G. Diau, *ACS Energy Lett.* **2022**, *7*, 4436–4442.
[14] E. W.-G. Diau, E. Jokar, M. Rameez, *ACS Energy Lett.* **2019**, *4*, 1930–1937.
[15] S. Vegiraju, W. Ke, P. Priyanka, J. S. Ni, Y. C. Wu, I. Spanopoulos, S. L. Yau, T. J. Marks, M. C. Chen, M. G. Kanatzidis, *Adv. Funct. Mater.* **2019**, *29*, 1905393.
[16] W. Ke, P. Priyanka, S. Vegiraju, C. C. Stoumpos, I. Spanopoulos, C. M.M. Soe, T. J. Marks, M.-C. Chen, M. G. Kanatzidis, *J. Am. Chem. Soc.* **2018**, *140*, 388–393.
[17] C. H. Kuan, R. Balasaravanan, S. M. Hsu, J. S. Ni, Y. T. Tsai, Z. X. Zhang, M. C. Chen, E. W.G. Diau, *Adv. Mater.* **2023**, *35*, 2300681.
[18] A. Velusamy, S. N. Afraj, S. Yau, C. L. Liu, Y. Ezhumalai, P. Kumaresan, M. C. Chen, *Journal of the Chinese Chemical Society* **2022**, *69*, 1253–1275.
[19] R. Balasaravanan, C. H. Kuan, S. M. Hsu, E. C. Chang, Y. C. Chen, Y. T. Tsai, M. L. Jhou, S. L. Yau, C. L. Liu, M. C. Chen, *Adv. Energy Mater.* **2023**, *13*, 2302047.
[20] B. B. Yu, Z. Chen, Y. Zhu, Y. Wang, B. Han, G. Chen, X. Zhang, Z. Du, Z. He, *Adv. Mater.* **2021**, *33*, 2102055.
[21] N. Sun, W. Gao, H. Dong, Y. Liu, X. Liu, Z. Wu, L. Song, C. Ran, Y. Chen, *ACS Energy Lett.* **2021**, *6*, 2863–2875.
[22] A. Babayigit, D. DuyThanh, A. Ethirajan, J. Manca, M. Muller, H.-G. Boyen, B. Conings, *Sci. Rep.* **2016**, *6*, 18721.
[23] Y. Shi, Z. Zhu, D. Miao, Y. Ding, Q. Mi, *ACS Energy Lett.* **2024**, *9*, 1895–1897.
[24] E. Jokar, H.-S. Chuang, C.-H. Kuan, H.-P. Wu, C.-H. Hou, J.-J. Shyue, E. Wei-GuangDiau, *J. Phys. Chem. Lett.* **2021**, *12*, 10106–10111.
[25] X. Jiang, F. Wang, Q. Wei, H. Li, Y. Shang, W. Zhou, C. Wang, P. Cheng, Q. Chen, L. Chen, *Nat. Commun.* **2020**, *11*, 1245.
[26] X. Jiang, Z. Zang, Y. Zhou, H. Li, Q. Wei, Z. Ning, *Accounts of Materials Research* **2021**, *2*, 210–219.
[27] E. Jokar, P.-Y. Cheng, C.-Y. Lin, S. Narra, S. Shahbazi, E. Wei-GuangDiau, *ACS Energy Lett.* **2021**, *6*, 485–492.
[28] E. Jokar, P. H. Hou, S. S. Bhosale, H. S. Chuang, S. Narra, E. Wei-GuangDiau, *ChemSusChem* **2021**, *14*, 4415–4421.
[29] E. Jokar, Z. Y. Huang, S. Narra, C. Y. Wang, V. Kattoor, C. C. Chung, E. W.G. Diau, *Adv. Energy Mater.* **2018**, *8*, 1701640.
[30] C.-M. Tsai, Y.-P. Lin, M. K. Pola, S. Narra, E. Jokar, Y.-W. Yang, E. W.-G. Diau, *ACS Energy Lett.* **2018**, *3*, 2077–2085.
[31] X. Jiang, H. Li, Q. Zhou, Q. Wei, M. Wei, L. Jiang, Z. Wang, Z. Peng, F. Wang, Z. Zang, *J. Am. Chem. Soc.* **2021**, *143*, 10970–10976.
[32] E. Jokar, C.-H. Chien, A. Fathi, M. Rameez, Y.-H. Chang, E. W.-G. Diau, *Energy Environ. Sci.* **2018**, *11*, 2353–2362.
[33] E. Jokar, C. H. Chien, C. M. Tsai, A. Fathi, E. W.G. Diau, *Adv. Mater.* **2019**, *31*, 1804835.
[34] Z. Zhu, X. Jiang, D. Yu, N. Yu, Z. Ning, Q. Mi, *ACS Energy Lett.* **2022**, *7*, 2079–2083.
[35] W. Han, G. Ren, J. Liu, Z. Li, H. Bao, C. Liu, W. Guo, *ACS Appl. Mater. Interfaces* **2020**, *12*, 49297–49322.
[36] C.-H. Kuan, G.-S. Luo, S. Narra, S. Maity, H. Hiramatsu, Y.-W. Tsai, J.-M. Lin, C.-H. Hou, J.-J. Shyue, E. W.-G. Diau, *Chem. Eng. J.* **2022**, *450*, 138037.
[37] X. Liu, T. Wu, X. Luo, H. Wang, M. Furue, T. Bessho, Y. Zhang, J. Nakazaki, H. Segawa, L. Han, *ACS Energy Lett.* **2021**, *7*, 425–431.
[38] S. Shahbazi, M.-Y. Li, A. Fathi, E. W.-G. Diau, *ACS Energy Lett.* **2020**, *5*, 2508–2511.
[39] R. Shang, Z. Zhou, H. Nishioka, H. Halim, S. Furukawa, I. Takei, N. Ninomiya, E. Nakamura, *J. Am. Chem. Soc.* **2018**, *140*, 5018–5022.
[40] A. Al-Ashouri, A. Magomedov, M. Roß, M. Jošt, M. Talaikis, G. Chistiakova, T. Bertram, J. A. Márquez, E. Köhnen, E. Kasparavičius, *Energy Environ. Sci.* **2019**, *12*, 3356–3369.
[41] G. Kapil, T. Bessho, Y. Sanehira, S. R. Sahamir, M. Chen, A. K. Baranwal, D. Liu, Y. Sono, D. Hirotani, D. Nomura, *ACS Energy Lett.* **2022**, *7*, 966–974.
[42] E. Aktas, N. Phung, H. Köbler, D. A. González, M. Méndez, I. Kafedjiska, S.-H. Turren-Cruz, R. Wenisch, I. Lauermann, A. Abate, *Energy Environ. Sci.* **2021**, *14*, 3976–3985.
[43] F. Ali, C. Roldán-Carmona, M. Sohail, M. K. Nazeeruddin, *Adv. Energy Mater.* **2020**, *10*, 2002989.
[44] Y. Bai, Q. Dong, Y. Shao, Y. Deng, Q. Wang, L. Shen, D. Wang, W. Wei, J. Huang, *Nat. Commun.* **2016**, *7*, 12806.
[45] Ç. Kırbıyık, K. Kara, D. A. Kara, M. Z. Yiğit, B. Istanbullu, M. Can, N. S. Sariciftci, M. Scharber, M. Kuş, *Appl. Surf. Sci.* **2017**, *423*, 521–527.
[46] A. Ullah, K. H. Park, H. D. Nguyen, Y. Siddique, S. Shah, H. Tran, S. Park, S. I. Lee, K. K. Lee, C. H. Han, *Adv. Energy Mater.* **2022**, *12*, 2103175.
[47] R. Azmi, W. T. Hadmojo, S. Sinaga, C. L. Lee, S. C. Yoon, I. H. Jung, S. Y. Jang, *Adv. Energy Mater.* **2018**, *8*, 1701683.

[48] K. Wang, J. Liu, J. Yin, E. Aydin, G. T. Harrison, W. Liu, S. Chen, O. F. Mohammed, S. DeWolf, *Adv. Funct. Mater.* **2020**, *30*, 2002861.
[49] K. Yang, Q. Liao, J. Huang, Z. Zhang, M. Su, Z. Chen, Z. Wu, D. Wang, Z. Lai, H. Y. Woo, *Angew. Chem. Int. Ed.* **2022**, *61*, e202113749.
[50] L. Duan, Y. Chen, J. Yuan, X. Zong, Z. Sun, Q. Wu, S. Xue, *Dyes Pigm.* **2020**, *178*, 108334.
[51] D. Bharath, M. Sasikumar, N. R. Chereddy, J. R. Vaidya, S. Pola, *Sol. Energy* **2018**, *174*, 130–138.
[52] K. Rakstys, S. Paek, P. Gao, P. Gratia, T. Marszalek, G. Grancini, K. T. Cho, K. Genevicius, V. Jankauskas, W. Pisula, *J. Mater. Chem. A* **2017**, *5*, 7811–7815.
[53] J. Kastner, H. Kuzmany, D. Vegh, M. Landl, L. Cuff, M. Kertesz, *Macromolecules* **1995**, *28*, 2922–2929.
[54] D. D. Kenning, S. C. Rasmussen, *Macromolecules* **2003**, *36*, 6298–6299.
[55] L. Wen, B. C. Duck, P. C. Dastoor, S. C. Rasmussen, *Macromolecules* **2008**, *41*, 4576–4578.
[56] G. Sonmez, C. K. Shen, Y. Rubin, F. Wudl, *Angew. Chem.* **2004**, *116*, 1524–1528.
[57] G. Sonmez, C. K. Shen, Y. Rubin, F. Wudl, *Adv. Mater.* **2005**, *17*, 897–900.
[58] F. Zhang, E. Perzon, X. Wang, W. Mammo, M. R. Andersson, O. Inganäs, *Adv. Funct. Mater.* **2005**, *15*, 745–750.
[59] J. Li, J. Yang, J. Hu, Y. Chen, B. Xiao, E. Zhou, *Chem. Commun.* **2018**, *54*, 10770–10773.
[60] W. Chen, Y. Zhou, G. Chen, Y. Wu, B. Tu, F. Z. Liu, L. Huang, A. M.C. Ng, A. B. Djurišić, Z. He, *Adv. Energy Mater.* **2019**, *9*, 1803872.
[61] S. Seo, S. Jeong, C. Bae, N. G. Park, H. Shin, *Adv. Mater.* **2018**, *30*, 1801010.
[62] J. Xu, C. C. Boyd, Z. J. Yu, A. F. Palmstrom, D. J. Witter, B. W. Larson, R. M. France, J. Werner, S. P. Harvey, E. J. Wolf, *Science* **2020**, *367*, 1097–1104.
[63] C. C. Boyd, R. Cheacharoen, K. A. Bush, R. Prasanna, T. Leijtens, M. D. McGehee, *ACS Energy Lett.* **2018**, *3*, 1772–1778.
[64] S. Zhang, F. Ye, X. Wang, R. Chen, H. Zhang, L. Zhan, X. Jiang, Y. Li, X. Ji, S. Liu, *Science* **2023**, *380*, 404–409.
[65] B. Li, C. Zhang, D. Gao, X. Sun, S. Zhang, Z. Li, J. Gong, S. Li, Z. Zhu, *Adv. Mater.* **2023**, 2309768.
[66] S. N. Afraj, C. C. Lin, A. Velusamy, C. H. Cho, H. Y. Liu, J. Chen, G. H. Lee, J. C. Fu, J. S. Ni, S. H. Tung, *Adv. Funct. Mater.* **2022**, *32*, 2200880.
[67] C.-C. Lin, S. N. Afraj, A. Velusamy, P.-C. Yu, C.-H. Cho, J. Chen, Y.-H. Li, G.-H. Lee, S.-H. Tung, C.-L. Liu, *ACS Nano* **2020**, *15*, 727–738.
[68] A. Velusamy, C. H. Yu, S. N. Afraj, C. C. Lin, W. Y. Lo, C. J. Yeh, Y. W. Wu, H. C. Hsieh, J. Chen, G. H. Lee, *Adv. Sci.* **2021**, *8*, 2002930.
[69] S. N. Afraj, B.-H. Jiang, Y.-W. Su, C.-H. Yang, H.-S. Shih, A. Velusamy, J.-S. Ni, Y. Ezhumalai, T.-Y. Su, C.-L. Liu, S. Yau, C.-P. Chen, M.-C. Chen, *J. Mater. Chem. C* **2024**, *12*, 2247–2257.
[70] Y.-D. Lin, K.-M. Lee, S. H. Chang, T.-Y. Tsai, H.-C. Chung, C.-C. Chou, H.-Y. Chen, T. J. Chow, S.-S. Sun, *ACS Appl. Energ. Mater.* **2021**, *4*, 4719–4728.
[71] M. Bonomo, A. G. Marrani, V. Novelli, M. Awais, D. P. Dowling, J. G. Vos, D. Dini, *Appl. Surf. Sci.* **2017**, *403*, 441–447.
[72] A. Zhang, M. Li, C. Dong, W. Ye, Y. Zhu, J. Yang, L. Hu, X. Li, L. Xu, Y. Zhou, *Chem. Eng. J.* **2024**, *494*, 153253.
[73] Y. Koshtyal, D. Nazarov, I. Ezhov, I. Mitrofanov, A. Kim, A. Rymyantsev, O. Lyutakov, A. Popovich, M. Maximov, *Coating* **2019**, *9*, 301.
[74] M. B. Islam, M. Yanagida, Y. Shirai, Y. Nabetani, K. Miyano, *ACS Omega* **2017**, *2*, 2291–2299.
[75] S. Yu, Z. Xiong, H. Zhou, Q. Zhang, Z. Wang, F. Ma, Z. Qu, Y. Zhao, X. Chu, X. Zhang, *Science* **2023**, *382*, 1399–1404.

Manuscript received: April 16, 2024
Accepted manuscript online: July 8, 2024
Version of record online: ■■, ■■

Research Article

Solar Cells

C.-H. Kuan, S. N. Afraj, Y.-L. Huang, A. Velusamy, C.-L. Liu, T.-Y. Su, X. Jiang, J.-M. Lin, M.-C. Chen,* E. W.-G. Diau* _____ **e202407228**

Functionalized Thienopyrazines on NiOx Film as Self-Assembled Monolayer for Efficient Tin-Perovskite Solar Cells Using a Two-Step Method

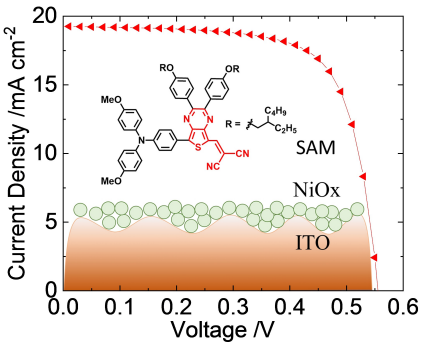

Three thienopyrazine-based organic molecules as self-assembled monolayers (SAMs) were developed and deposited on NiOx films for tin-based perovskite solar cells. Using NiOx as interlayer can modify the hydrophilicity and surface roughness of the ITO substrate. The two-step method was applied to enable better quality of the tin perovskite layer grown on the NiOx/SAM substrates, ultimately achieving a power conversion efficiency of 7.7%.